Correlating exciton localization with compositional fluctuations in InGaN/GaN quantum wells grown on GaN planar surfaces and facets of GaN triangular prisms

S. Khatsevich and D. H. Rich[a)]
Department of Physics, Ilse Katz Center for Meso and Nanoscale Science and Technology, Ben-Gurion University of the Negev, P.O. Box 653, Beer-Sheva 84105, Israel

X. Zhang and P. D. Dapkus
Compound Semiconductor Laboratory, Department of Electrical Engineering/Electrophysics, University of Southern California, Los Angeles, California 90089, USA

(Received 21 May 2007; accepted 7 September 2007; published online 2 November 2007)

We have used spatially and temporally resolved cathodoluminescence (CL) to study the carrier recombination dynamics of InGaN quantum wells (QWs) grown on (0001)-oriented planar GaN and $\{1\bar{1}01\}$-oriented facets of GaN triangular prisms prepared by lateral epitaxial overgrowth in a metal-organic chemical vapor deposition system. The effects of In migration during growth on the resulting QW thickness and composition were examined. We employed a variable temperature time-resolved CL imaging approach that enables a spatial correlation between regions of enhanced exciton localization, luminescence efficiency, and radiative lifetime with the aim of distinguishing between excitons localized in In-rich quantum dots and those in the surrounding Ga-rich QW regions. © *2007 American Institute of Physics*. [DOI: 10.1063/1.2802291]

I. INTRODUCTION

Advancements in the growth, doping, and processing of InGaN/GaN quantum wells (QWs) and heterostructures have led to ultrabright light emitting diodes and functional lasers for the current generation *blu-ray* optical disk storage.[1,2] Despite the rapidly growing consumer markets for such applications, many issues still remain regarding stoichiometric fluctuations in ternary InGaN thin films that lead to submicron fluctuations in the alloy composition, as a result of a miscibility gap at relevant growth temperatures.[3–6] The tendency of InGaN layers to decompose into distinct regions of in-plane In- and Ga-rich phases (i.e., spinodal decomposition) will subsequently lead to the formation of In-rich quantum dots (QDs).[7–9] Sharp excitonic emission lines from individual InGaN QDs have been observed, including lines originating from the biexciton formation.[8,10] Polarized emission lines from excitonic complexes in single InGaN/GaN QDs have recently been reported.[11] While it may be possible to exploit spinodal decomposition in ternary films to create QDs that will lead to exciton localization and an enhanced radiative recombination for lasing, there is also clearly a desire to fabricate thin InGaN films and QWs whose phase separation is minimal and in-plane In composition is homogenous.

The method of lateral epitaxial overgrowth (LEO) has shown great promise in reducing the threading dislocation density in thick films to a level of $\sim 10^4$ cm^{-2} in GaN.[12–15] The issue of the role of threading dislocations and their associated strain fields in creation of spinodally decomposed (In- and Ga-phase separated regions) is still an open issue. In this paper, we report on the spatial variation in excitonic localization phenomena of InGaN/GaN single quantum wells (SQWs) prepared using LEO and conventional planar growth on the (0001) plane. In particular, we examine a sample in LEO where the resulting shape of the LEO structure is a triangular prism, having facet orientations of $\{1\bar{1}01\}$. The growth of InGaN QWs on such a LEO triangular prism structure and the resulting variations in the QW composition and thickness were previously examined with low-temperature cathodoluminescence (CL) imaging and spectroscopy with steady-state excitation.[16] In this paper, we present a time-resolved study to further augment the results of Ref. 16 and, in particular, focus on the effect of spatial variations in excitonic localization that relate directly to regions exhibiting In-rich QD formation. We employ a variable temperature time-resolved CL imaging approach that enables a spatial correlation between regions of enhanced exciton localization, luminescence efficiency, and radiative lifetime with the aim of distinguishing between regions of zero-dimensional (0D) and two-dimensional (2D) excitonic confinements.

II. EXPERIMENTAL

A. Sample growth

The growth of GaN triangular prisms on *c*-plane (0001) sapphire using LEO has been described previously in detail.[14,15] In LEO a dielectric mask is deposited over a starting GaN buffer layer which may contain a relatively high defect density. The mask is patterned using standard photolithography and reactive ion etching to create selective openings in the mask that possess a desired geometry or orientation relative to the GaN. Subsequent GaN growth then occurs in the opening in both vertical and lateral directions over the dielectric mask thereby minimizing the vertical

[a)]Electronic mail: danrich@bgu.ac.il

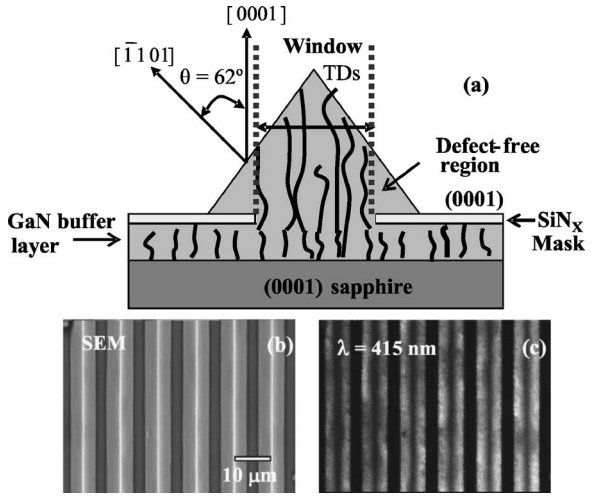

FIG. 1. Schematic illustration of the LEO technique and partial suppression of threading dislocations (wavy lines in illustration) during LEO growth. Stripe patterning along the $\langle 11\bar{2}0\rangle_{GaN}$ directions results in LEO stripes with a triangular cross section (a). θ is the angle between the QW's growth direction and the [0001] *c*-axis direction. Plan-view SEM and monochromatic CL images (λ=415 nm) are shown in (b) and (c), respectively. The electron beam excitation conditions were E_B=15 keV and I_B=125 pA at T=166 K.

propagation of threading dislocations attendant in the GaN growth on an as-prepared low-temperature buffer layer. Having achieved relatively defect-free regions of GaN, subsequent growth of higher quality InGaN/GaN QWs can be performed. Metal-organic chemical vapor deposition (MOCVD) was used to grow GaN buffer layers on the sapphire substrate, followed by deposition of a 170 nm thick SiN_x mask using plasma-enhanced CVD. Conventional photolithography and reactive ion etching were used to form patterned stripes along the $[11\bar{2}0]$ direction, possessing openings with widths of 4 μm and pitch of 10 μm. The LEO GaN was then grown over the SiN_x mask at a temperature of 1000 °C for ~1 h, resulting in triangular prisms possessing $\{1\bar{1}01\}$ sidewalls, as illustrated in Fig. 1. Subsequently, a nominal 4 nm thick $In_{0.15}Ga_{0.85}N$ QW at 775 °C was grown and capped with a 70 nm thick GaN layer. The nominal 15% In composition represents an average composition for an InGaN film grown on a flat (0001) GaN buffer. A plan-view scanning electron micrograph and a monochromatic CL image of the sample are shown in Figs. 1(b) and 1(c). Transmission electron microscopy (TEM) of this sample has been previously reported.[16] We have prepared a reference sample without the SiN mask that contains a 4 nm thick $In_{0.15}Ga_{0.85}N$ QW on a flat (0001) GaN buffer layer, followed by a 70 nm thick GaN capping layer.

B. A modified time-resolved cathodoluminescence approach

The CL experiments were performed with a JEOL-5910 scanning electron microscope (SEM) using a 15 keV electron beam with probe current in the 0.03–40 nA range. An ultraviolet multialkali photomultiplier tube operating in the 185–850 nm spectral range enabled photon counting of the luminescence that was dispersed by a 0.25 m monochromator. Measurements were performed at different temperatures in the 50–310 K temperature range. Time-resolved CL experiments were performed with the method of delayed coincidence in an inverted single photon counting mode, with a maximum time resolution of ~100 ps.[17] Electron beam pulses of 50 ns width with a 1 MHz repetition rate were used to excite the sample. Steady-state and time-delayed CL spectra were acquired with a spectral resolution of 1 nm.

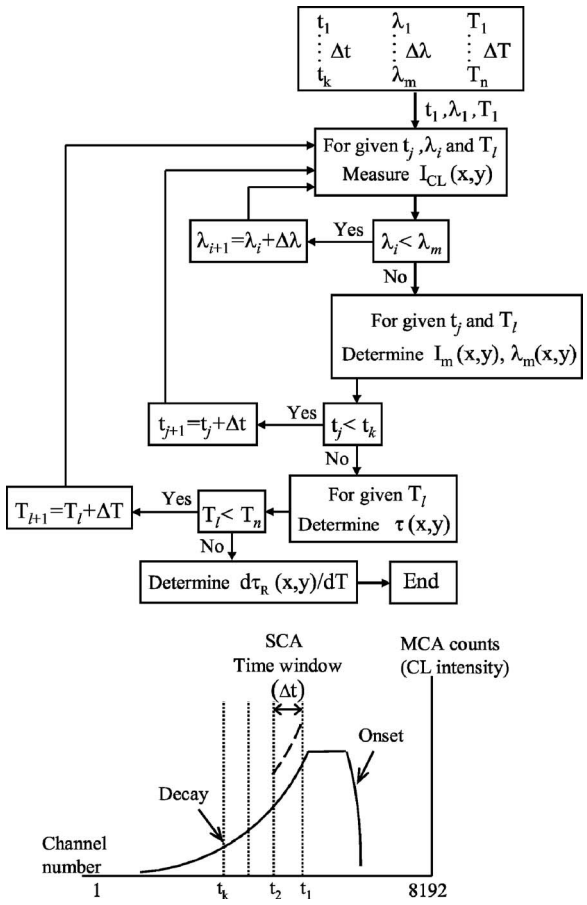

FIG. 2. Schematic illustration of the experimental time-resolved CL technique that was employed to measure spatial variations in the decay lifetime and the temperature dependence of the radiative lifetime, which enables a determination of the exciton dimensionality (i.e., 0D vs 2D). A multichannel analyzer was used to determine the full CL decay transients for a fixed electron beam position, while a single channel analyzer was used to acquire monochromatic CL images at fixed time windows relative to the decay edge of the excitation pulse. Additional details regarding the CL detection system are provided in Ref. 17.

A modified experimental approach was used to measure spatial variations in the decay lifetime and to determine the exciton dimensionality (i.e., 2D versus 0D) as a function of position for various temperatures, as illustrated in Fig. 2. A series of discrete monochromatic CL images or one-dimensional (1D) line scans at different wavelengths was first acquired in a set of previously defined time windows, with time width Δt and position t_j relative to the decay edge of the excitation pulse. This is followed by a construction of the local CL spectrum at each of the (x,y) scan points and a determination of the maximum CL intensity I_m (peak intensity), corresponding peak wavelength λ_m, and thus leads to the mapping $\lambda_m(x,y)$. The same procedure is repeated for each time window, as shown in Fig. 2. The decay lifetime is

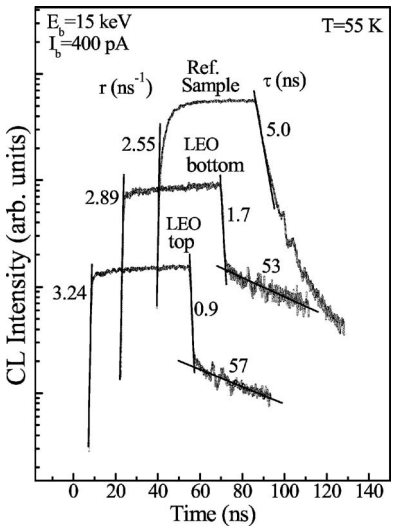

FIG. 3. CL transients (intensity vs time) of the QW peak emission. The transients show the onset and decay of the QW peak luminescence acquired from excitation at the bottom and top of the triangular prisms in the LEO patterned sample and for the reference unpatterned sample for $E_b=15$ keV and $I_b=400$ pA at $T=55$ K. Initial onset rates, r, and decay times, τ, obtained by a linear fit from the slopes of the onset and decay curves are indicated for each sample. Two different decay times, obtained by a linear fit of the two respective slopes in the decay curve, are indicated for the LEO sample.

then determined in the usual manner by constructing $\ln(I_m)$ versus time (t_j) plots and using a least squares fitting procedure for each spatial scan point (x,y) to determine the mapping of the CL decay time, $\tau(x,y)$. In general, this decay lifetime will also depend on the emission wavelength λ, and we therefore obtained $\lambda_m(x,y)$ so that $\tau(x,y,\lambda_m)$ could be determined for a fixed temperature. Finally, the same procedures were repeated for various temperatures in the 55–80 K range, thereby enabling a determination of $\tau(x,y,T)$. Consequently, a linear fit at each point yielded the slope $\partial\tau(x,y,T)/\partial T$, which we then use to evaluate the dimensionality (2D versus 0D) of the system.

III. RESULTS AND DISCUSSION

A. CL lifetime and onset rate measurements

In order to study the temporal behavior of the SQW luminescence, the initial onset and decay CL transients of the SQW peak emission were acquired for the LEO and reference samples at different temperatures. Spatially averaged CL intensity versus time transients of the SQW peak luminescence acquired for different regions of the LEO patterned sample and for reference unpatterned sample with a beam energy of 15 keV and beam current of 400 pA at $T=55$ K are shown in Fig. 3. In order to detect and measure SQW luminescence from the bottom and the top of the triangular prism, the sharply focused electron beam was rastered over a 128×96 nm^2 region in respective areas of the LEO patterned sample. For the reference unpatterned sample, the SQW emission was acquired while the electron beam was rastered over a 128×96 μm^2 region. To quantify the initial increase in the CL intensity with time, the onset rates, $r=\Delta\ln(I_{CL})/\Delta t$, given by the slopes of the tangents to the onset curves, are defined as shown in Fig. 3 for the onset part of the CL transients. The initial onset rates measured at $T=55$ K are 3.24, 2.89, and 2.55 ns^{-1} for the LEO top and bottom regions and for reference unpatterned sample, respectively, as indicated in Fig. 3. The luminescence decay times τ are measured from the slopes in the decay part of the $\ln(I_{CL})$ versus time transients of the SQW peak, as indicated in Fig. 3. Two different slopes in the decay curve are observed for the SQW peak emission of the LEO patterned sample, and two different decay times, obtained by a linear fit of the two respective slopes, are indicated, as shown. The initial decay time of $\tau_1=0.9$ ns (1.7 ns), obtained by a linear fit of the initial slope in the decay curve, is followed by a significantly longer decay time of $\tau_2=57$ ns (53 ns), as seen from Fig. 3 for the top (bottom) region of the prism.

The initial slope of the decay curve corresponds to the excitonic emission from the SQW, while the second slope corresponds to the impurity-related emission that stems from the GaN region, as will be shown later in this section. A significantly longer initial decay time of $\tau=5$ ns is obtained for the reference unpatterned sample. As will be discussed in Sec. III C, the decay lifetimes at temperatures below 60 K are close to the radiative lifetimes of free or localized excitons. In the simple one particle picture, the radiative lifetime is related to the square of the overlap integral of electron and hole wave functions $\psi_e(z_e)$ and $\psi_h(z_h)$. An increase in the electron-hole wave function overlap results in a decrease of the radiative lifetime. A comparison of the LEO and reference samples shows that these samples have nominally the same average In composition of ~15%, but different QW thickness. Previously, we determined using TEM that QW widths in this LEO sample vary from $L_{QW}\approx4$ nm at the bottom of the triangular prism, which is similar to the QW width of the reference sample, to $L_{QW}\approx6$ nm at the top.[16] Using a theoretical model, we determined previously that In composition in the LEO sample varies from $x\approx0.1$ at the bottom to $x\approx0.19$ at the top of the prism.[16] The increase in the In composition will result in the increase of the strain-induced piezoelectric polarization and field. This increase in the electric field will lead to a decrease in the overlap integral and will result in the increased values of the radiative lifetime. This effect is consequently more pronounced for thicker QWs.[18] Thus, longer radiative lifetimes and longer decay lifetimes at low temperatures are expected for the QW peak emission of the LEO sample for regions near the apex of the triangular prisms. The opposite result, namely, a longer decay lifetime obtained for the reference sample at low temperatures (as seen in Fig. 3), strongly suggests that the electric field in the LEO sample is diminished relative to that in the reference sample. A theoretical calculation of the strain-induced piezoelectric polarization shows a significant reduction in both the electric field and radiative lifetime of excitons as the QW growth direction changes from [0001] to $[1\bar{1}01]$, which is the direction of the QW growth on the prism faces in the LEO sample.[19]

B. Time-delayed CL spectra measurements

In order to further study the temporal behavior of the QW luminescence and to examine the relaxation and collec-

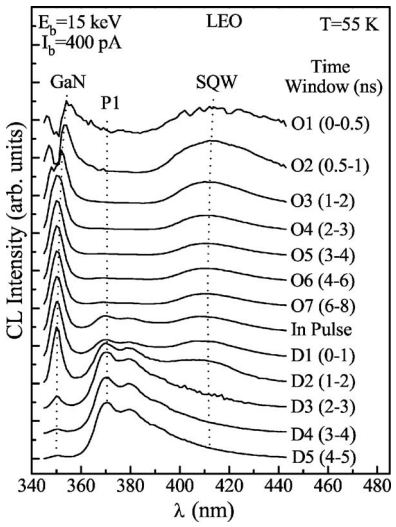

FIG. 4. Time-delayed CL spectra acquired for the LEO patterned sample at $T=55$ K for $E_b=15$ keV and $I_b=400$ pA. The spectra are shown with various onset (Oi) and decay (Di) time windows. All spectra are normalized to have about the same maximum peak height. Different emission peaks and wavelength positions are indicated. The doublet labeled P1 is identified as a free electron to acceptor transition in bulk GaN. During the onset stage of the luminescence only small changes in the SQW peak position are observed.

tion of carriers into the QW, time-delayed CL spectra were obtained for the LEO and reference samples at $T=55$ K, as shown in Figs. 4 and 5. All spectra are renormalized to have about the same maximum peak height. The time windows O1–O7 and D1–D8 denote time windows relative to the beginning of onset and decay, respectively, of the luminescence, as referred to the beginning and end of the electron beam pulses. The constant excitation spectra, which were measured in the center of the 50 ns excitation pulse, are labeled *in pulse*, as indicated in Figs. 4 and 5. Different emis-

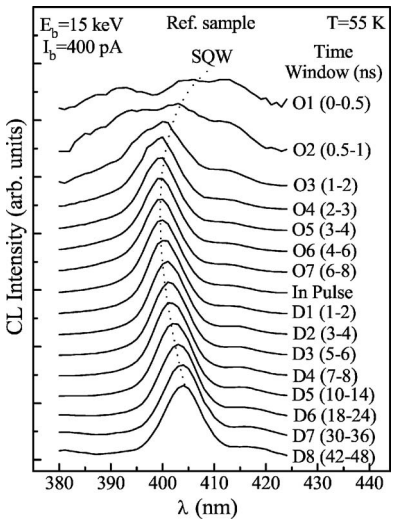

FIG. 5. Time-delayed CL spectra of the QW emission for the reference unpatterned sample acquired for $E_b=15$ keV and $I_b=400$ pA at $T=55$ K. The spectra are shown with various onset (Oi) and decay (Di) time windows. All spectra are normalized to have about the same maximum peak height. A vertical dotted line indicates both a blue- and a redshift of ~40 meV in the QW peak position during the onset and decay stages of the luminescence, respectively.

sion peaks are indicated in the time-delayed CL spectra obtained for the LEO sample, as seen in Fig. 4. The doublet labeled P1 was identified as originating from a free electron to acceptor transition in bulk GaN.[20] The rapid rise of the QW peak at the shortest time window O1 (centered at 250 ps) reflects the rapid capture of carriers into the QW from the GaN buffer layer. During the onset stage of the luminescence, the SQW peak line shape remains nearly constant and only a small spectral diffusion of ~8 meV is observed, indicating that carrier filling and screening are negligible in the LEO sample under the present excitation conditions. During the decay stage of the luminescence the QW peak emission decays rapidly in the time windows D1–D3 and is then masked by emission of peak P1, which dominates in the CL spectra in the later time windows, as seen in Fig. 4. As follows from the direct comparison of Figs. 3 and 4, the initial slope in the decay curve obtained for the QW peak emission of the LEO sample corresponds to the emission that stems from the QW region, while the second slope with a significantly longer decay lifetime corresponds to the impurity-related emission of peak P1. It was determined by depth-resolved measurements (not shown) that the impurity-related emission of peak P1 emanates mainly from GaN layers below the QW.

In order to accentuate the differences in behavior of the LEO and reference samples, Fig. 5 shows only a part of time-delayed CL spectra containing the QW peak. A slower rise and a longer decay of the QW peak luminescence are observed for the reference sample relative to that obtained for the LEO sample, as seen from Figs. 4 and 5. A large phase-space filling, screening of the field, and consequently a reduction of the quantum confined Stark effect (QCSE) with time towards higher transition energies during the onset stage and spectral diffusion towards lower energies of ~40 meV during the decay stage of the QW peak luminescence are indicated in Fig. 5 with a vertical dotted line. For spectra acquired under steady-state and approximately constant excitation conditions (labeled as *in pulse* in Figs. 4 and 5) the carrier density in the QW can be sufficient to partially screen the internal field and reduce the QCSE.[21,22] During the decay stage of the luminescence, the screening of the field decreases due to the loss of excess carriers by various decay processes. The increase in the internal electric field leads to a redshifting of the QW emission, as seen in Fig. 5. The absence of such spectral diffusion in the time-resolved CL spectra of the LEO sample might serve as yet another indication that the electric field is diminished in that sample.

C. Correlating composition variations, dimensionality, and exciton localization

A strong spatial variation in the peak wavelength of the QW emission was observed previously for the LEO patterned sample.[16] Thus in order to determine the spatial variation in the decay lifetime correctly, a measurement of the decay lifetime at peak wavelength is of crucial importance. By performing the procedures described in Sec. II B and illustrated in Fig. 2 at different temperatures, the radiative lifetime and temperature dependence of the radiative lifetime, which determines the exciton dimensionality, can be mea-

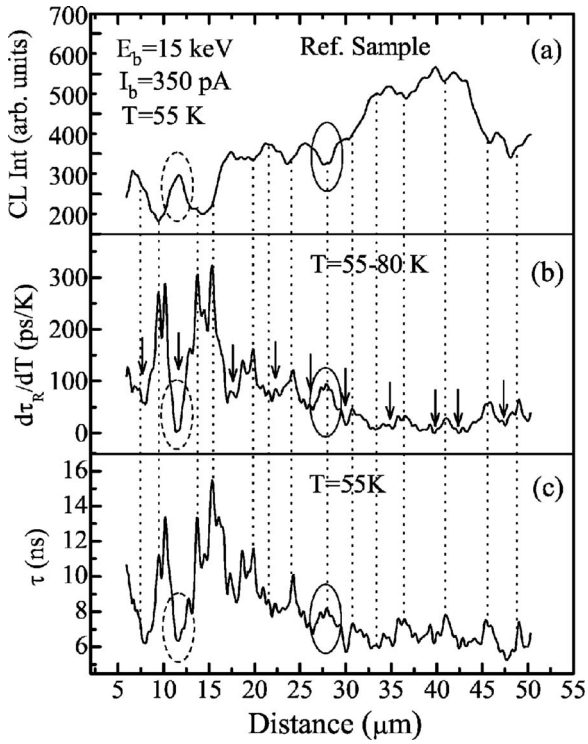

FIG. 6. Results of low-temperature line-scan measurements for the reference unpatterned InGaN QW sample showing: (a) integrated CL intensity of QW emission at $T=55$ K, (b) temperature dependence of the radiative lifetime, $\partial\tau_R/\partial T$, determined at QW peak wavelengths in the 55–80 K range and (c) decay lifetime, τ, measured at QW peak wavelengths for $T=55$ K vs distance along an arbitrary line. The vertical dashed lines illustrate the spatial correlation between peaks and dips for these scans. Positions of increased localization are indicated in (b) with arrows. Two typical regions exhibiting enhanced and reduced localizations are illustrated with dashed and solid ovals, respectively.

sured at each scan point. The radiative lifetime at each scan point at a given temperature can be estimated from the combined measurement of the decay lifetime, and the peak CL intensity, I_m, acquired under steady-state and approximately constant excitation conditions (labeled as *in pulse* in Figs. 4 and 5) using a standard expression for the radiative efficiency η as follows:[23,24]

$$\eta(T) = \frac{\tau(T)}{\tau_R(T)} = \frac{I_m(T)}{I_{m0}}, \tag{1}$$

where I_{m0} is equal to the value of the saturated CL intensity at low temperatures. The temperature dependence of the radiative lifetime,$\partial\tau_R/\partial T$, at each scan point can be determined from a τ_R versus T plot by a least square fitting procedure. The linear increase in τ_R with T at low temperatures is an unambiguous signature of a two-dimensional excitonic system, consistent with radiative recombination of free excitons,[25–27] while a temperature independent behavior is expected for highly localized excitons.[25]

Results of the low-temperature line-scan measurements for the reference unpatterned sample are shown in Fig. 6. The vertical dotted lines help us illustrate the spatial correlation between peaks and dips for each of the parameters I_{CL}, $\partial\tau_R/\partial T$, and τ. Emission of both weakly and highly localized excitons, with different degrees of localization, is observed. Positions of highly localized excitons with $\partial\tau_R/\partial T \approx 0$ are indicated in Fig. 6(b) with arrows. The strong correspondence between positions of the localization maxima (minima), where dips (peaks) in $\partial\tau_R/\partial T$ are observed, maxima (minima) of the integrated CL intensity, and minima (maxima) of the decay lifetime measured at low temperatures is observed in Fig. 6. Two typical regions exhibiting enhanced and reduced localizations are illustrated with dashed and solid ovals, respectively, in Fig. 6. These spatial correlations can be understood through the following simple model. An increase in the exciton localization will lead to an increase in the electron and hole wave function overlap. Moreover, local reductions in the band gap caused by an enhanced In concentration will lead to an increase in the local carrier density collected in these phase separated regions. The increase in the electron and hole wave function overlap will likewise reduce the radiative lifetime. The integrated CL intensity is inversely proportional to the τ_R and is given by $I_{CL} \propto |\int_{-\infty}^{\infty} dz \psi_e(z_e)\psi_h(z_h)|^2$. Both an increase in the overlap integral and an increase in the collected local carrier density will lead to increased values of the integrated CL intensity, as seen in Fig. 6. Previously, we showed that positions of maximal CL intensity are correlated with local redshifts in wavelength for a planar InGaN QW sample,[6,16] thereby demonstrating that regions of enhanced localization are further consistent with local enhancement in the In concentration (i.e., an In-rich region).

Figure 7 shows results of the low-temperature line-scan measurements for the LEO patterned sample. The vertical dotted lines help us to illustrate correlation between peaks and dips for these scans. In Fig. 7(b), which shows a line scan of $\partial\tau_R/\partial T$ at peak emission wavelengths, the positions of highly localized excitons are indicated with arrows. The apexes of the triangular prisms are identified by the peaks of the secondary electron intensity, I_{SE}. From the lower edges of the prism, the decay lifetime, τ, measured at the QW peak wavelengths for $T=55$ K decreases from $\tau \approx 3$ ns near the bottom to $\tau \approx 0.8$ ns near the top, as seen from Fig. 7(c). The decay lifetime measured at this temperature should be sufficiently close to the radiative lifetime of free or localized excitons, as inferred from a comparison of Figs. 7(c) and 8(b) which shows a reversal of the lifetime behavior observed for the LEO sample at low and high temperatures, respectively. The initial decrease in the decay lifetime throughout the lower through middle regions of the QW on the prism is well correlated with the decrease in $\partial\tau_R/\partial T$, which corresponds to an increase in the exciton localization, and is accompanied by a simultaneous increase in the integrated CL intensity, I_{CL}, and peak wavelength, λ_m. Also, two typical regions of enhanced and reduced localizations are shown with dashed and solid ovals, respectively, in Fig. 7 to better illustrate these correlations.

Correlations between I_{CL}, $\partial\tau_R/\partial T$, and τ can be explained by the same simple qualitative model, which was used to explain results obtained from the reference sample. A noticeable increase in both λ_m and $\partial\tau_R/\partial T$ is observed as the electron beam approaches the apex of the prism. The relative increase in λ_m suggests a strong connection with the increase in both In composition and QW width. The latter is supported by the TEM measurements, which showed an increase

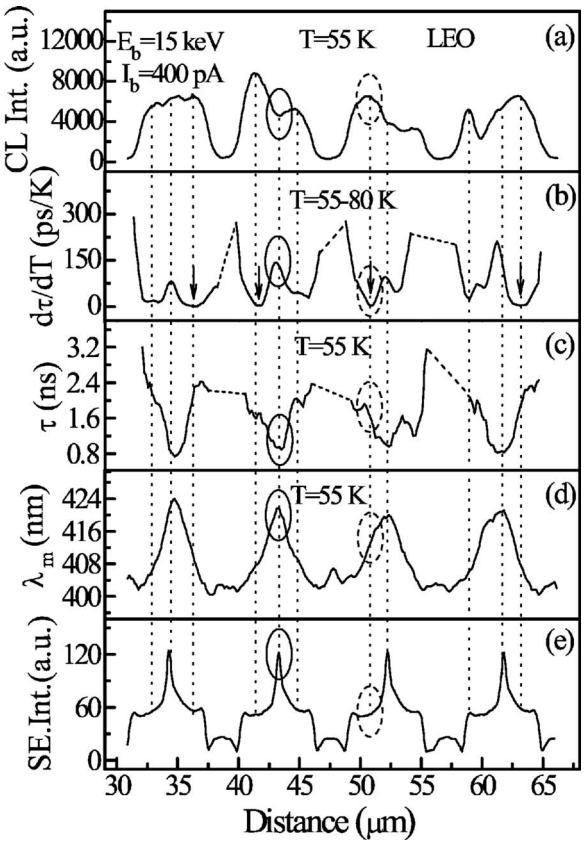

FIG. 7. Results of low-temperature line-scan measurements for the LEO patterned InGaN QW sample showing: (a) integrated CL intensity of QW emission at $T=55$ K, (b) temperature dependence of the radiative lifetime, $\partial\tau_R/\partial T$, determined at QW peak wavelengths in the 55–80 K range, (c) decay lifetime, τ, measured at QW peak wavelengths for $T=55$ K, (d) the peak wavelength λ_m, and (e) secondary electron intensity vs distance along an arbitrary line in $[1\bar{1}00]$ direction. The vertical dashed lines illustrate the spatial correlation between peaks and dips for these scans. Positions of increased localization (i.e., nearly 0D excitons) are indicated in (b) with arrows. Two typical regions of enhanced and reduced localizations are shown with dashed and solid ovals, respectively.

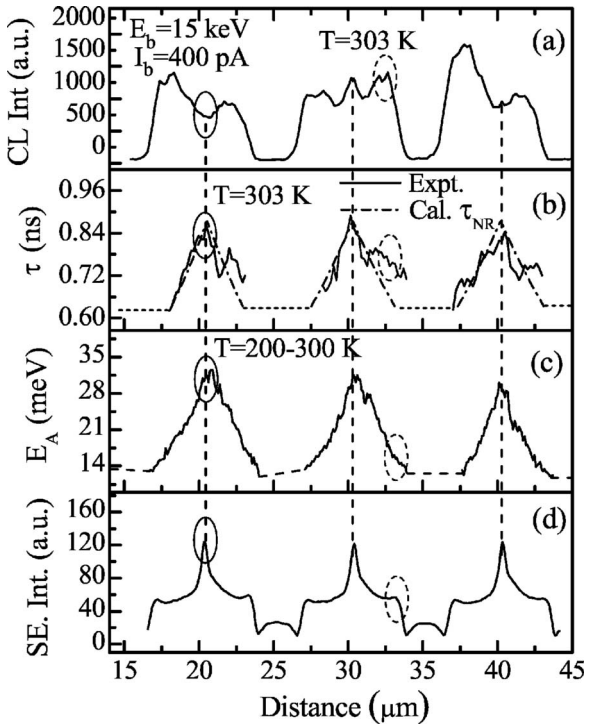

FIG. 8. Results of high-temperature line-scan measurements for the LEO patterned InGaN QW sample showing: (a) integrated CL intensity of QW emission at $T=303$ K, (b) decay lifetime, τ, measured at QW peak wavelengths for $T=303$ K, (c) activation energy E_A determined from thermal quenching measurements of the peak CL intensity in the temperature range of 200–300 K (from Ref. 16), and (d) secondary electron intensity vs distance along an arbitrary line in the $[1\bar{1}00]$ direction. The vertical dashed lines illustrate the spatial correlation between peaks and dips for these scans. The dash-dot lines in (b) show results of model calculation for nonradiative lifetimes, τ_{NR}, as a function of position. Two typical regions of enhanced and decreased nonradiative rates are illustrated with dashed and solid ovals, respectively.

in the QW width from $L_{QW}\approx 4$ nm at the bottom to $L_{QW}\approx 6$ nm at the top of the triangular prism.[16] In previous studies of InGaN/GaN QW samples, a strong increase in $\partial\tau_R/\partial T$ with the QW width was observed.[25] The observed increase in $\partial\tau_R/\partial T$ with the QW width is most likely caused by decrease of the exciton localization.[19,28] In contrast, an increase in the In composition will lead to a decrease in the QW band gap, resulting in increased effective barrier heights for electrons and holes and an increased exciton localization. Thus, the increase in $\partial\tau_R/\partial T$, as seen in Fig. 7(b), is most likely caused by increased values of the QW width near the top. An increase in the In composition will lead to an increase in the strain-induced piezoelectric field, which tends to separate the electron and hole wave functions towards the opposite sides of the well. Both the increase in the QW width and the increase in the In composition will lead to a decrease of the overlap integral, resulting in longer radiative lifetimes, which should be observed near the top of the prism. However, this contradicts the results of Fig. 7(c), showing a progressive decrease in the decay lifetime from the bottom to the top of the prism. In order to explain the observed discrepancy between theory and experiment, a nonintuitive assumption concerning the decrease in electric field from the bottom to the top of the prism is needed. We can attribute this decrease to be due to the strain relaxation that will be especially strong near the apex of the triangular prisms. TEM of the LEO sample showed an enhanced propagation of threading dislocations near the prism apex together with the localization of Y-band emission near the top, suggesting a strain relaxation that occurs through such threading dislocations.[16,29]

We further note that in the case of triangular prisms, a 1D localization near the apex could be expected due to the abrupt changes in the InGaN QW width and In composition relative to that in the sidewall QWs. Quantum wires have been fabricated previously by utilizing such a facet-dependent growth so as to control cation migration rates along the facets and alter the cross-sectional geometry of the wire.[30,31] However, the present measurements are unable to distinguish between 1D and 2D localizations since we performed a linear fit over a relatively narrow temperature range in which distinguishing between $\sqrt{T}$ and T dependencies in the radiative lifetime could not be performed reliably.

Figure 8 shows results obtained for the LEO patterned sample at $T=303$ K. The vertical dotted lines help us to illustrate correlations between peaks and dips for these scans. The apexes of the prisms are identified by the peaks of the

secondary electron intensity, I_{SE}. From the lower edges of the prism, the decay lifetime increases from $\tau \approx 0.6$ ns at the bottom to $\tau \approx 0.9$ ns at the top, as seen in Fig. 8(b). This is to be compared with results of Fig. 7(c), showing a reversal of the lifetime behavior observed at low temperatures. The measured decay lifetime τ at temperature T is related to the radiative and nonradiative recombination rates, $R_R \propto \tau_R^{-1}$ and $R_{NR} \propto \tau_{NR}^{-1}$, respectively, by $R_t \propto \tau^{-1}$ where $R_t = R_R + R_{NR}$ is the total recombination rate. The nonradiative recombination rate has the following temperature dependence:

$$R_{NR} = R_{NR0} e^{-E_A/k_B T}, \tag{2}$$

where R_{NR0} is a coefficient independent of temperature and E_A is the energy of the thermally activated process.[24] The radiative recombination rate R_R is either temperature independent or decreases as the temperature increases, owing to the increase in τ_R. At sufficiently low temperatures, R_{NR} becomes very small approaching zero, as seen from Eq. (2), so that $R_{NR} \approx 0$ and $R_t \approx R_R$ indicating that radiative recombination process becomes dominant. At high temperatures $R_{NR} \gg R_R$ and $R_t \approx R_{NR}$, thus recombination is governed by nonradiative recombination processes.[32] A reversal of the lifetime behavior observed by direct comparison of Figs. 7(c) and 8(b) strongly suggests that two different processes are responsible for the low- and high-temperature lifetime behaviors observed for QW emission of the LEO sample, namely, radiative recombination process at low temperatures, $\tau \approx \tau_R$, and nonradiative processes at high temperatures, $\tau \approx \tau_{NR}$.

The following simple model is proposed in order to explain spatial variations in the decay lifetime at high temperatures, as seen in Fig. 8(b). The radiative recombination rate, R_R, is assumed independent of temperature for high temperatures (~200–300 K), while the temperature dependence of the nonradiative recombination rate is given by Eq. (2). Thus, Eq. (1) for the radiative efficiency η can be expressed in the following form:[24]

$$\eta(T) = \frac{R_R}{R_R + R_{NR0} \exp(-E_A/k_B T)} = \frac{I(T)}{I_0}. \tag{3}$$

At high temperatures $R_{NR} \gg R_R$ and, by denoting $I_0 R_R / R_{NR0} \equiv C$, Eq. (3) becomes $I(T) = C \exp(E_A/k_B T)$. This result indicates an Arrenhius dependence with constant activation energy E_A in the expected thermal quenching of luminescence for high temperatures. The spatial dependence of E_A, as determined from thermal quenching measurements in the 200–300 K temperature range, is shown in Fig. 8(c), as obtained from Ref. 16. The measured activation energies increase from $E_A \approx 14$ meV at the bottom to $E_A \approx 30$ meV at the top of the prism. The nonradiative lifetimes were then calculated by substitution of these experimentally measured activation energies into the equation $\tau_{NR} = \tau_{NR0} \exp(E_A/k_B T)$ in which τ_{NR0} is assumed independent of position. τ_{NR0} was determined by fitting the calculated nonradiative lifetime to the decay lifetime, $\tau \approx 0.6$ ns, measured at the bottom of the prism. The results of the calculation are shown in Fig. 8(b) with dash-dotted lines for $T = 303$ K. These results exhibit a strong correspondence between the measured decay lifetime τ at high temperatures and the calculated nonradiative lifetime τ_{NR} as observed from Fig. 8(b). Thus, the correspondence strongly suggests that the same thermal activation process is responsible for: (i) The decrease in the QW luminescence and (ii) the lifetime behavior observed for the LEO sample at high temperatures. Two typical regions of enhanced and decreased nonradiative rates and their associated spatial correlations are illustrated in Fig. 8 with dashed and solid ovals, respectively. Previously, we demonstrated the existence of a strong correlation between the observed thermal activation energy E_A and the calculated exciton binding energy E_B for various positions along InGaN/GaN QWs grown on GaN triangular prisms, suggesting exciton dissociation is responsible for the observed temperature dependence of the QW luminescence in the high temperature range of ~200–300 K.[16] We can further extend this model by concluding that the nonradiative recombination lifetime and rate are similarly linked to thermally enhanced exciton dissociation at high temperatures.

IV. SUMMARY AND CONCLUSIONS

We have used spatially and temporally resolved CL to study the carrier recombination dynamics of InGaN QWs grown on (0001)-oriented planar GaN and $\{1\bar{1}01\}$-oriented facets of GaN triangular prisms prepared by LEO. We employed a variable temperature time-resolved CL imaging approach to examine spatial correlations between regions of exciton localization, varying luminescence efficiency, decay lifetime, and activation energy. The objective was to distinguish between regions where excitons are localized in In-rich quantum dots and conversely where recombination occurs in the surrounding Ga-rich regions. The establishment of 0D exciton localization using the enhanced approach is a fundamental result which should have bearing on future studies of localization and QD formation by spinodal decomposition in the InGaN/GaN thin film system. A thermally activated nonradiative recombination model was invoked to explain a reversal in the spatial dependence of lifetime between cases of high and low temperatures, in which we show that nonradiative recombination is linked to an enhanced exciton dissociation at high temperatures.

ACKNOWLEDGMENTS

This work was supported in part by the Israel Science Foundation (ISF Grant No. 8/02-1), NSF, ARO, ONR, and DARPA through the National Center for Integrated Photonic Technology (NCIPT).

[1] S. Nakamura, M. Senoh, S. Nagahama, N. Iwasa, T. Yamada, T. Matsushita, H. Kiyoku, and Y. Sigimoto, Appl. Phys. Lett. **68**, 2105 (1996).
[2] S. Nakamura, G. Fasol, and S. Pearton, *The Blue Laser Diode* (Springer, Berlin, 2000).
[3] S. Chichibu, K. Wada, and S. Nakamura, Appl. Phys. Lett. **71**, 2346 (1997).
[4] Y. Narukawa, Y. Kawakami, M. Funato, S. Fujita, S. Fujita, and S. Nakamura, Appl. Phys. Lett. **70**, 981 (1997).
[5] T. Riemann, D. Rudloff, J. Christen, A. Krost, M. Lunenburger, H. Protzmann, and M. Heuken, Phys. Status Solidi B **216**, 301 (1999).
[6] X. Zhang, D. H. Rich, J. T. Kobayashi, N. P. Kobayashi, and P. D. Dapkus, Appl. Phys. Lett. **73**, 1430 (1998).
[7] S. Chichibu, T. Azuhata, T. Sota, and S. Nakamura, Appl. Phys. Lett. **69**, 4188 (1996).

[8]I. L. Krestnikov, N. N. Ledentsov, A. Hoffmann, D. Bimberg, A. V. Sakharov, W. V. Lundin, A. F. Tsatsul'nikov, A. S. Usikov, Zh. I. Alferov, Yu. G. Musikhin, and D. Gerthsen, Phys. Rev. B **66**, 155310 (2002).
[9]H. Gotoh, T. Akasaka, Y. Kobayashi, T. Makimoto, and H. Nakano, Solid State Commun. **138**, 590 (2006).
[10]R. Seguin, S. Rodt, A. Strittmatter, L. Reißmann, T. Bartel, A. Hoffmann, D. Bimberg, E. Hahn, and D. Gerthsen, Appl. Phys. Lett. **84**, 4023 (2004).
[11]M. Winkelnkemper, R. Seguin, S. Rodt, A. Schliwa, L. Reißmann, A. Strittmatter, A. Hoffmann, and D. Bimberg, J. Appl. Phys. **101**, 113708 (2007).
[12]T. S. Zheleva, O.-H. Nam, M. D. Bremser, and R. F. Davis, Appl. Phys. Lett. **71**, 2472 (1997).
[13]N. P. Kobayashi, J. T. Kobayashi, X. Zhang, P. D. Dapkus, and D. H. Rich, Appl. Phys. Lett. **74**, 2836 (1999).
[14]X. Zhang, P. D. Dapkus, and D. H. Rich, Appl. Phys. Lett. **77**, 1496 (2000).
[15]P. Vennegues, B. Beaumont, V. Bousquet, M. Vaille, and P. Gibart, J. Appl. Phys. **87**, 4175 (2000).
[16]S. Khatsevich, D. H. Rich, X. Zhang, W. Zhou, and P. D. Dapkus, J. Appl. Phys. **95**, 1832 (2004).
[17]H. T. Lin, D. H. Rich, A. Konkar, P. Chen, and A. Madhukar, J. Appl. Phys. **81**, 3186 (1997).
[18]J. S. Im, H. Kollmer, J. Off, A. Sohmer, F. Scholz, and A. Hangleiter, Phys. Rev. B **57**, R9435 (1998).
[19]S. Khatsevich, Ph.D. thesis, 2007.
[20]S. N. Mohammad and H. Morkoc, Prog. Quantum Electron. **20**, 361 (1996).
[21]P. Lefebvre, S. Kalliakos, T. Bretagnon, P. Valvin, T. Taliercio, B. Gil, N. Grandjean, and J. Massies, Phys. Rev. B **69**, 035307 (2004).
[22]S. Kalliakos, P. Lefebvre, and T. Taliercio, Phys. Rev. B **67**, 205307 (2003).
[23]R. C. Miller, D. A. Kleinman, W. A. Nordland, Jr., and A. C. Gossard, Phys. Rev. B **22**, 863 (1980).
[24]J. I. Pankove, *Optical Processes in Semiconductors* (Dover, New York, 1971).
[25]E. Berkowicz, D. Gershoni, G. Bahir, E. Lakin, D. Shilo, E. Zolotoyabko, A. C. Abare, S. P. Denbaars, and L. A. Coldren, Phys. Rev. B **61**, 10994 (2000).
[26]L. C. Andreani, F. Tassone, and F. Bassani, Solid State Commun. **77**, 641 (1991).
[27]P. Lefebvre, J. Allegre, B. Gil, A. Kavokine, H. Mathieu, W. Kim, A. Salvador, A. Botchkarev, and H. Morkoc, Phys. Rev. B **57**, R9447 (1998).
[28]A. Sasaki, K. Nishizuka, T. Wang, S. Sakai, A. Kaneta, Y. Kawakami, and Sg. Fugita, Solid State Commun. **129**, 31 (2004).
[29]F. A. Ponce, D. P. Bour, W. Gotz, and P. J. Wright, Appl. Phys. Lett. **68**, 57 (1996).
[30]E. Kapon, K. Kash, E. M. Clausen, D. M. Hwang, and E. Colas, Appl. Phys. Lett. **60**, 477 (1992).
[31]V. Pérez-Solórzano, A. Gröning, H. Schweizer, and M. Jetter, Phys. Status Solidi B **242**, R97 (2005).
[32]M. S. Minsky, S. B. Fleischer, A. C. Abare, J. E. Bowers, E. L. Hu, S. Keller, and S. P. Denbaars, Appl. Phys. Lett. **72**, 1066 (1998).